Available online at www.sciencedirect.com

ScienceDirect

journal homepage: www.elsevier.com/locate/he

Strategies to improve the catalytic activity of Fe-based catalysts for nitrogen reduction reaction

Giuseppe Tranchida [a,b], *Rachela Gabriella Milazzo* [a,*], *Marco Leonardi* [a,b], *Silvia Scalese* [a], *Luca Pulvirenti* [b], *Guido G. Condorelli* [b], *Corrado Bongiorno* [a], *Salvatore Lombardo* [a], *Stefania M.S. Privitera* [a]

[a] *CNR-IMM VIII Strada 5, 95121, Catania (CT), Italy*

[b] *Dipartimento di Scienze Chimiche, Università di Catania and INSTM UdR Catania, Viale Andrea Doria 6, 95125, Catania, Italy*

HIGHLIGHTS

- Fe-based NPs are deposited by drop casting and chemical reduction on C-cloth substrates.
- Particles morphology has been optimized.
- The catalytic activity for Nitrogen electroreduction reaction was investigated.
- A crucial role is played by the oxygen vacancies and by the Fe+2/Fe+3 ratio.
- The ammonia yield with the optimized catalyst was 5 times higher than without optimization.

GRAPHICAL ABSTRACT

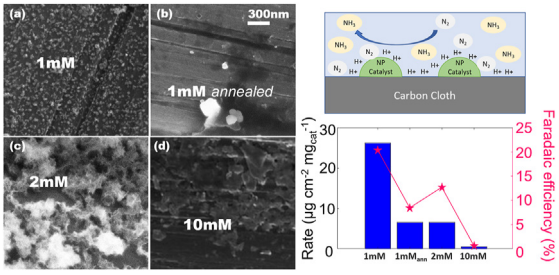

ARTICLE INFO

Article history:
Received 15 November 2022
Received in revised form
4 February 2023
Accepted 15 March 2023
Available online 5 April 2023

Keywords:
Catalysts
Iron-based nanoparticles
Oxygen vacancies

ABSTRACT

Electrochemical ammonia synthesis from N_2 under mild condition is considered a promising strategy to store energy produced by renewable sources, but it is affected by the lack of efficient catalysts for nitrogen reduction. In this work Fe-based nanoparticles with different morphology are deposited on carbon cloth via drop-casting and chemical reduction. The catalyst activity has been evaluated by cyclic voltammetry and chronoamperometry, using a 0.01 M phosphate buffered electrolyte (PBS). The produced ammonia has been determined through the indophenol method. As effective strategy to improve the catalytic activity, the morphology and particle size have been optimized and an electrochemical activation procedure has been implemented. Activation increases the available active sites and is related to higher amount of oxygen vacancies and Fe^{+2}/Fe^{+3} ratio. Catalysts with optimized morphology produce ammonia at −0.35 V vs RHE with yield

* *Corresponding author.*
E-mail address: gabriella.milazzo@imm.cnr.it (R.G. Milazzo).

https://doi.org/10.1016/j.ijhydene.2023.03.241

0360-3199/© 2023 The Authors. Published by Elsevier Ltd on behalf of Hydrogen Energy Publications LLC. This is an open access article under the CC BY-NC-ND license (http://creativecommons.org/licenses/by-nc-nd/4.0/).

Nitrogen electroreduction reaction
Green ammonia synthesis

of 26.44 μg $mg_{cat}^{-1}h^{-1}$ and Faradaic efficiency of 20.4%, more than five times higher than without activation.

© 2023 The Authors. Published by Elsevier Ltd on behalf of Hydrogen Energy Publications LLC. This is an open access article under the CC BY-NC-ND license (http://creativecommons.org/licenses/by-nc-nd/4.0/).

Introduction

Ammonia (NH_3) is not only an important chemical, largely essential in agriculture as fertilizer, as well as for plastics and pharmaceuticals, but it is also a promising energy vector, because of its high hydrogen content, high volumetric energy density and easy of liquefaction for storage [1–3]. Industrial production of ammonia mainly relies on the well consolidated Haber-Bosch process [4], that requires high temperatures (350–550 °C) and high pressures (150–350 atm) to make efficient the reaction between nitrogen and hydrogen gases ($N_2 + 3H_2 \rightarrow 2NH_3$, $\Delta_f H^0 = -91.8$ kJ mol^{-1}) and it is responsible for massive CO_2 generation, roughly corresponding to about 2% of worldwide emissions [5,6].

Nitrogen reduction reaction (NRR) to ammonia obtained through electrocatalytic processes (e-NRR) is considered an interesting alternative since it offers the possibility of directly using water as hydrogen source and it can be conducted at ambient temperature and pressure [7–9]. Despite the great interest and the efforts that have been made to improve the ammonia formation yield rate, the electrochemical synthesis of ammonia is still at a nascent stage and it faces many drawbacks [9]. The e-NRR mechanism is quite complex and still unclear, even if many efforts have been devoted to the elucidations of its highlights. One major challenge for nitrogen reduction is the low selectivity due to the competing hydrogen evolution reduction (HER). This usually determines low Faradaic Efficiency (FE) for nitrogen reduction, since a large number of electrons is used for hydrogen evolution, whilst only a small fraction is used for reducing nitrogen. To overcome the selectivity challenge, an optimal catalyst should be able to enhance the e-NRR activity and suppress the activity of the competing HER. Theoretical studies based on Density Functional Theory (DFT) calculations provide predictions on catalysts materials and morphology, such as the effects of defects, facet and surface functionalization [10–14].

Recent works have demonstrated the potentiality of transition metals (TM) for e-NRR, thanks to the presence of *d* orbital electrons and unoccupied orbitals suitable for activating the strong N≡N triple bond [15]. In particular, noble metals such as Au, Rh and Ru have been adopted for the e-NRR reaction, with yield rate up to about 3.6 μg mg_{cat}^{-1} h^{-1} for Ru and Faradaic Efficiency of 13.36% for Au, with a top NH_3 yield rate of 9.43 μg mg_{cat}^{-1} h^{-1} [16–22]. However, the use of earth abundant catalysts would be preferable for a sustainable and circular economy [23,24]. Among these, iron is attractive since it is abundant and plays a key role in biological nitrogenase for natural N_2 fixation, so there is growing interest in Fe based catalyst and its oxides, where the intrinsic HER activity could be suppressed. For instance Fe/Fe_3O_4, Fe_3O_4/Ti have shown Faradaic efficiencies of 8.29% and 2.6% and rate of 0.19 μg h^{-1} cm^{-2} or 3.42 μg h^{-1} cm^{-2}, respectively [25–28]. Single atom catalysts (SACs) made of isolated single Fe atomic sites anchored to N-doped carbon frameworks have shown a yield rate of 62.9 μg mg_{cat}^{-1} h^{-1} [29]. With the aim to understand the relevant physical parameters and to improve the ammonia yield at low temperature, several approaches have been proposed. Introducing more oxygen vacancies to the hematite surface has been reported to improve the NRR performance, reaching production rate of 1.45 μg h^{-1} cm^{-2} and a NH_3 FE of 8.28% after the first 1 h chronoamperometry test, demonstrating the important role of the surface states in transition-metal oxides [30]. Controlling the wettability of the catalyst surface has been suggested as an effective method to improve the ammonia yield of reduced graphene oxide, obtaining increased efficiency with increasing hydrophobicity [31–38]. It is known that reducing the size of electrocatalysts to very small particles can be regarded as an efficient approach to achieve more catalytic active sites. Transition metal oxide nanodots have been fabricated for the NRR, exhibiting good electrocatalytic activities [29].

In this work, in order to improve the ammonia yield and efficiency of iron-based catalysts we adopt a double strategy consisting in (i) optimizing the catalyst morphology through the deposition conditions, and then (ii) promoting suitable surface states through electrochemical activation. Fe oxide nano-particles (NP) were deposited directly on carbon cloth substrate with a solution-based approach that makes only use of $FeCl_3$ and $NaBH_4$ and allows to tune the NP size by changing the Fe concentration in the deposition solution. The catalytic performance of the resulting NPs for the e-NRR has been evaluated by adopting an experimental protocol that enables a careful evaluation of all the environmental contaminations during ammonia synthesis experiments [9,39]. A strong correlation between the morphology and catalytic activity for NRR is found. Moreover, an efficient electrochemical activation procedure has been developed, allowing an improvement up to 5 times in the ammonia generation rate, which has been ascribed to the increased availability of oxygen vacancies.

Experimental section

Catalyst preparation

For the catalyst deposition we prepared several aqueous solutions with 1 mM, 2 mM and 10 mM of $FeCl_3$ (anhydrous, powder, ≥99.99% from Sigma Aldrich). A drop of 0.6 ml of each solution was placed on carbon cloth (AV Carb 1071 HCB) substrates (3 × 1.5) cm^2 on a hot plate at 80 °C. After water evaporation, substrates covered with the $FeCl_3$ powder were treated in $NaBH_4$ (powder, ≥98.0% from Sigma Aldrich) 100 mM for 60 s, at 21 °C while stirring the solution at 200 rpm.

After this step, samples were abundantly rinsed in deionized water and dried with air. Some samples were also annealed at 250 °C in air for 2 h. The amount of iron has been estimated by considering the $FeCl_3$ concentration and the drop volume. According to this, the maximum amount of deposited catalyst is almost 3.36×10^{-2} mg cm^{-2} for 1 mM $FeCl_3$. For higher concentrations the corresponding values were calculated accordingly.

Characterization

For the morphological, structural and chemical analyses we adopted a Scanning Electron Microscope (SEM) ZEISS SUPRATM 35. The same deposition procedure was replicated on a carbon grid for Transmission Electron Microscope (TEM) analyses with JEOL 2010F, equipped with a spectrometer GIF 2001 for electron energy loss (EELS) spectrum imaging and bright field (BF)/high angle annular detector (HAADF) for wide angle diffraction.

The electrochemical measurements, both cyclic voltammetry (CV) and chronoamperometry (CA), were carried out in a standard two compartments electrochemical cell using a Pt wire as counter electrode (CE) and a saturated calomel electrode (SCE, saturated KCl) as reference.

The conversion to the RHE reference scale is obtained using the following equation

$$E(\text{vs RHE}) = E(\text{vs SCE}) + 0.243 + 0.059 * \text{pH} \quad \text{Eq. 1}$$

The cathodic and the anodic compartments were filled with 22 ml and 8 ml respectively of 0.01 M phosphate buffer solution as electrolyte (PBS tablets by Fisher Scientific). Measurements have been performed by using a Keithley 2600-Source Current Unit.

X-ray photoelectron spectra (XPS) were acquired with a PHI 5600 multi-technique ESCA-Auger spectrometer equipped with a standard Mg Kα X-ray source. Samples were analyzed with a photoelectron take-off angle of 45° (relative to the sample surface) and with an acceptance angle of ±7°. The XPS binding energy scale was referenced by centering the C 1s peak at 285.0 eV.

Electrochemical ammonia synthesis

The experimental apparatus and procedure are described in Fig. 1a–b.

In this work we adopted a rigorous protocol to remove the external contaminations widely discussed in the literature [39,40]. The protocol includes the following steps.

(i) Before chronoamperometry experiments, both cell and electrodes were washed at 35 °C in water while stirring the solution at 150 rpm for 30 min.
(ii) N_2 and Ar gases with high purity (Nippon Gases 99.9999%) have been adopted and further purified by going through three saturators, placed before the cell, two of which were filled with 10 mM H_2SO_4 while the third contained only water. An additional acidic trap was placed after the gas outlet.
(iii) The electrolyte was analyzed before experiments (time T0), then we filled the cathode and the anode compartments respectively with 22 ml and 8 ml and we took 1 ml of the electrolyte out of the cell after 10 min (time T1) and 40 min (time T2) while keeping the circuit open and with nitrogen flow, to detect the ammonia already present in the cell, if any. If the NH_3 concentration was more than 10^{-6} M and/or it changed with time, the cell was emptied and rinsed again. This approach allowed a careful investigation of the possible contaminations originating inside the system, e. g. adventitious ammonia already present inside the electrode or in the cell.
(iv) Since the membrane can also be a source of contamination [41], Zirfon® PERL [42] has been employed instead of the commonly adopted proton exchange membrane, e.g. Nafion™.
(v) The ammonia amount evaluated from the UV-VIS absorbance in the solution at the open potential was subtracted from that measured after experiments with external voltage applied. The same measurements were done on both anodic and cathodic compartments but no NH_3 increase was detected at the anode.
(vi) Ar-saturated control experiments were performed at the same bias or with inactive catalysts as recommended in the literature [43]. The ammonia produced under Ar-saturated atmosphere was subtracted to the amount of ammonia produced in N_2 at the same conditions (voltage and time). Such a procedure allows the elimination of possible contributions, such as nitrates or nitrites, present in the water.

Ammonia measurements

Trisodium citrate dihydrate ($Na_3C_6H_5O_7 \cdot 2H_2O$ Alfa Aesar ≥99.0%), salicylic acid ($C_7H_6O_3$ Alfa Aesar 99%), sodium pentacyanonitrosylferrate (III) dihydrate nitroferricyanide ($Na_2[(-Fe(CN)_5NO] \cdot 2H_2O$ Alfa Aesar 98+%), ammonium chloride (NH_4Cl granular, Alfa Aesar 99.5%), sodium hypochlorite solution (NaClO, Alfa Aesar 11–15%) were used to measure the ammonia in the electrolyte by using the indophenol method.

The absorbance of the solution was detected at $\lambda = 660$ nm through an ultraviolet–visible (UV–vis) Bentham PVE300 spectrophotometer [44].

To calculate the amount of produced NH_3, the calibration curve was fitted using standard ammonia chloride solutions in the range between 0.25 and 0.022 μg mL^{-1}. Calibration solution were prepared with the same electrolyte (PBS 0.01 M) adopted during the experiments (See Fig. SI1). As a further control, the amount of ammonia has been also measured by adopting an ion selective electrode (ISE) by Orion. The comparison between values obtained with the two techniques is shown in the supplementary material.

Results and discussion

Fig. 2a-b and Fig. 2c-d shows the SEM micrographs of the carbon cloth electrodes obtained with 1 and 2 mM $FeCl_3$ respectively. Very small particles can be seen at high magnification in Fig. 2b. The mean size is about 38 nm (see Fig. SI 2). When the $FeCl_3$ concentration increases, the particles size

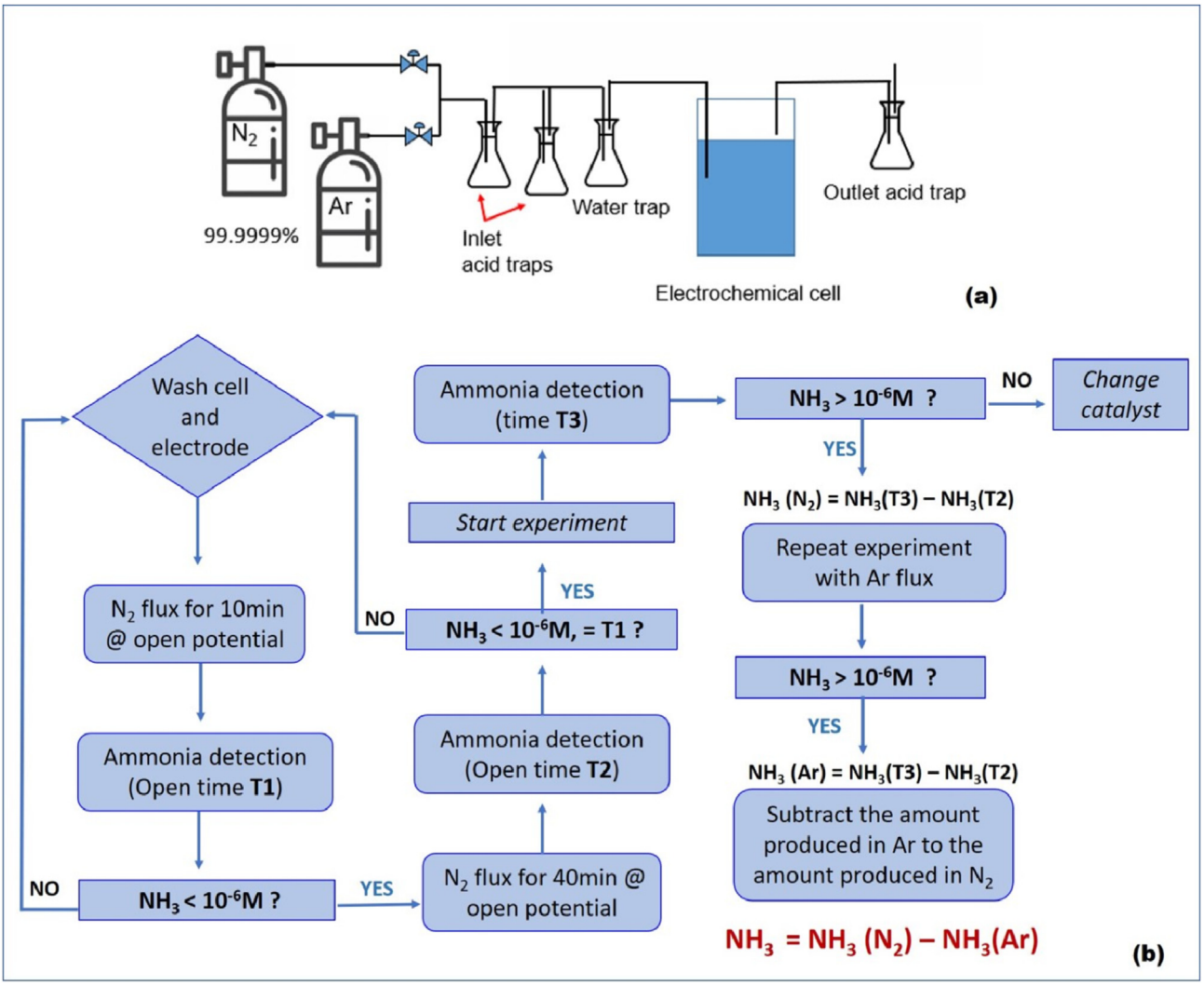

Fig. 1 – Schematic illustration of the e-NRR (a) electrocatalytic experimental system and (b) experimental protocol for ammonia determination.

increases too and coalescence produces an interconnected network, as it can be seen in Fig. 2d. Higher surface coverage and a smooth catalyst layer was obtained by deposition with the more concentrated solutions, 10 mM $FeCl_3$. Similar results were obtained also by annealing the 1 mM $FeCl_3$ sample in air at 250 °C for 2 h (see Fig. SI 3).

The electrochemical active surface area (EASA) has been evaluated by cyclic voltammetry method and under Ar flux. In a non-Faradaic region, we acquired a series of CV scans at different rates and the double layer capacitance (Cdl), directly related to the EASA, was computed from the slope of the linear regression between the current density differences (cathodic and anodic) in the middle of the potential window of CV curves versus the scan rates [45]. Results are shown in Fig. 3. The electrochemical analysis showed that a superior catalytically active surface area is associated to the electrode with the smallest particles size, deposited with 1 mM $FeCl_3$. Increasing the $FeCl_3$ concentration in the solution, as well as annealing of the sample, has not advantage in terms of active electrochemical sites: the values are all below 7.6 mF cm^{-2}, obtained for the 1 mM $FeCl_3$ solution. These results have been also confirmed by EIS (Fig. SI4 and SI_Table 1), with the highest double layer capacitance obtained for 1 mM $FeCl_3$.

The deposition procedure of 1 mM-Sample was replicated on a TEM C-grid and the crystalline structure of the nanoparticles was analyzed. Indeed, the amount of deposited Fe nanoparticles using 1 mM $FeCl_3$ is too low to be detected by X-ray diffraction, whilst the details of the composition can be obtained by high resolution TEM and EELS. XRD measurements of the sample prepared with 10 mM are shown in the supplementary material (Fig. SI5). Fig. 4a shows the EELS spectra acquired on two regions of the 1 mM $FeCl_3$ sample. In the area under investigation, we find that the shape of the L_3 edge of Iron changes locally. In region 1 the shape of the EELS spectrum can be typically ascribed (Fig. 4b) to Fe_2O_3 with two peaks, one at 709.3eV (see the arrows), attributed to a change in the oxidation state, and one at 710.8eV, more intense [46]. In region 2 instead, the spectrum exhibits a single peak at 710 eV, related to Fe_3O_4. We ascertained both Fe_2O_3 and Fe_3O_4, were deposited on our sample. Fig. 4c shows HRTEM acquired on a

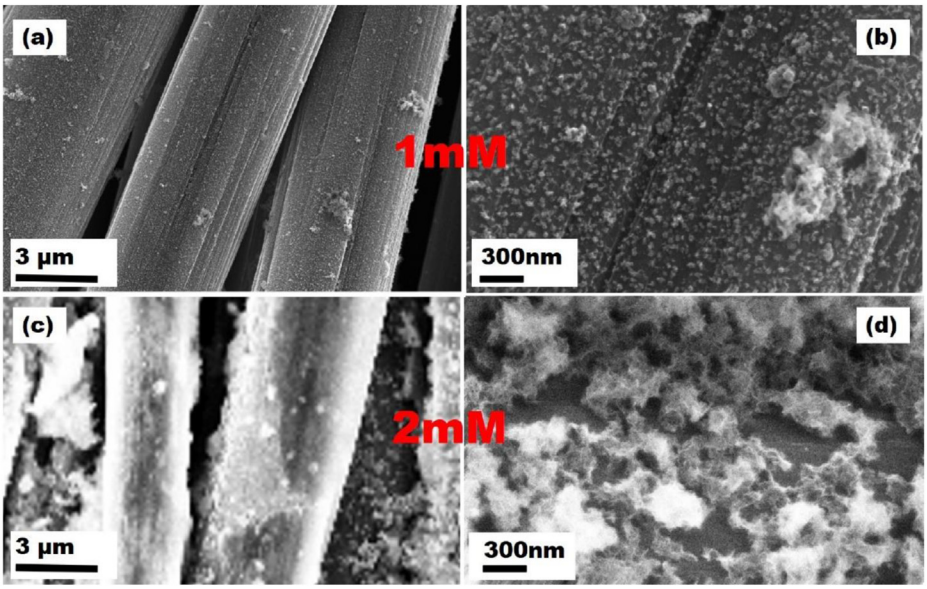

Fig. 2 – SEM micrographs at low and high magnifications of the AV Carb samples after deposition in $NaBH_4$ and (a–b) 1 mM, (c–d) 2 mM $FeCl_3$ respectively.

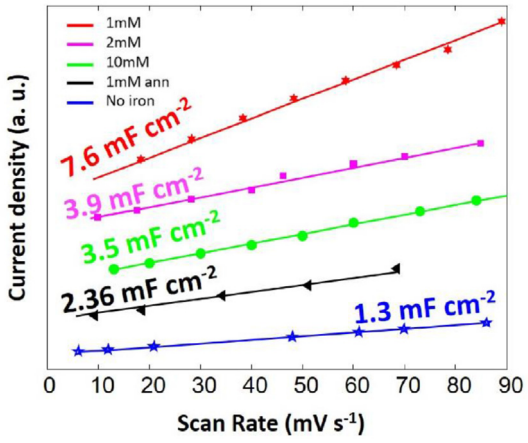

Fig. 3 – Double layer capacitance calculated from cyclic voltammetry for the carbon cloth samples loaded with Fe-based catalyst.

particle of region 2. The inset reports the fast Fourier transform (FFT) of the high-resolution image, with diffraction spots corresponding to the (222) and (400) crystalline planes of Fe_2O_3 with d-spacings of 2.41A and 2.08A, respectively. Fig. 4d reports the HRTEM acquired on a Fe_3O_4 particle; the corresponding FFT is shown in the inset, with spots ascribed to the (111) and the (220) planes, with a d-spacing of 2.52A and 2.9A, respectively [47,48]. After annealing, the morphology changes, with particles agglomeration and the formation of a smoother and more uniform coating. The composition is also modified, and the detected phase is mainly Fe_2O_3 (Fig. SI6).

The presence of both Fe_2O_3 and Fe_3O_4 in the 1 mM-Sample deposited on carbon cloth is confirmed by XPS analyses. Fig. 5a shows Fe 2p peaks of as deposited 1 mM sample. The catalyst is a mixture of Fe_3O_4 and Fe_2O_3, since peak 1 is related to Fe^{+2} of Fe_3O_4, peak 2 is typical in the Fe^{+3} of Fe_2O_3, peak 3 also is a satellite peak associated with Fe^{+3} of Fe_2O_3 [49–51]. The reduction of a part of Fe^{+3} to Fe^{+2} produces

Table 1 – Summary of NRR results reported in literature for iron based catalysts.

Catalyst	Experimental	NH_3 yield rate (μg cm^{-2} h^{-1})	NH_3 Yield rate (μg mg_{cat}^{-1} h^{-1})	FE(%)	Ref
Fe_2O_3/Fe_3O_4	0.01 M PBS	0.18	5.5	3.8	This work Before activation
Fe_2O_3/Fe_3O_4	0.01 M PBS	0.9	26.44	20.4	This work After activation
Fe/Fe_3O_4	0.1 M PBS	0.19		8.29	[25]
p-Fe_2O_3	0.1 M Na_2SO_4		13.56	7.69	[56]
Fe_2O_3	0.1 M Na_2SO_4		15.9	0.94	[57]
Fe-NPC	0.1 M NaOH		4.46	5.3	[58]
OV α Fe_2O_3	0.1 M KOH	0.46		6.04	[59]
Fe_2O_3 NPs	0.1 M Na_2SO_4		20	3.5	[60]
Fe_3O_4@rGo	0.1 M Na_2SO_4		28.01	11.47	[61]
M Fe_3O_4 NP	0.1 M Na_2SO_4		12.09	16.9	[62]
Fe_3O_4/Ti	0.1 M Na_2SO_4	3.42		2.6	[27]
Fe CNT	0.1 M KOH		34.83	9.28	[63]

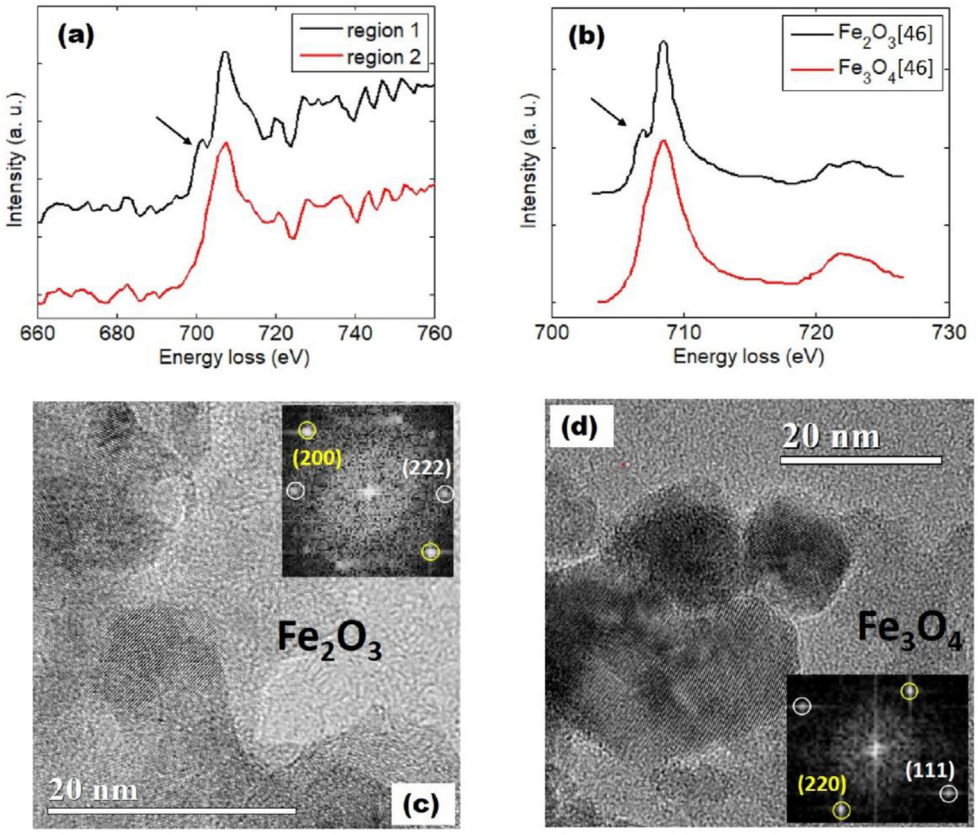

Fig. 4 – TEM analyses on nanoparticles obtained in the 1 mM $FeCl_3$ solution, (a) EELS spectrum for the L_3 edge of Iron acquired in two distinct regions of the TEM specimen and (b) literature data from Ref. [46]; (c–d) high resolution TEM on nanoparticles in regions 1 and 2 with the corresponding diffraction pattern [47,48].

oxygen vacancies, as it can be evidenced by the Oxygen XPS O1s signal (Fig. 5b), made by the convolution of two peaks, one at 529.9 eV, peak 1, typical of metal oxygen bond (OM), and peak 2, at 531.13 eV, corresponding to the oxygen vacancies [52]. Oxygen vacancies (OVs) are ubiquitous in metal oxides and have a pronounced effect on the physical and chemical properties of the material. Numerous strategies have been developed to create OVs in metal oxides, such as high temperature calcination, high energy particle bombardment, ion doping or chemical reduction (e. g. from H_2 or $NaBH_4$). The deposition method adopted in this study, including the chemical reduction by $NaBH_4$, is therefore expected to promote the OVs formation, whose presence has been reported to accelerate the charge/electron transfer rate, and therefore improving the electrocatalytic performance [14,52].

The catalyst activity and stability were analyzed by cyclic voltammetry (CV), with a scan rate of 15 mV s^{-1} under N_2 flux. We firstly adopted a potential range between +0.07 V and −0.45 V vs RHE. The corresponding curve, labeled as CV1, is

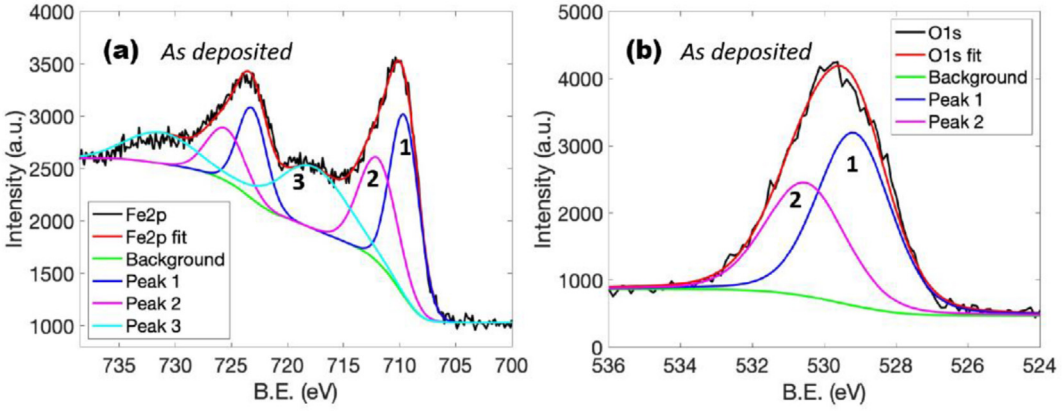

Fig. 5 – XPS spectra for Fe 2p in the 1 mM $FeCl_3$ as-deposited samples on carbon cloth.

shown in Fig. 6a. The voltage was applied according to the arrows, from the positive to the most negative in a direct scan and vice-versa in the reverse one. Each scan was repeated 4 times. After CV1 we performed the chronoamperometry (CA1) at −0.33 V vs RHE, shown in Fig. 6b and evaluated the produced ammonia after 40 min. During the CA1 the absolute value of the cathodic current initially decreases as a function of time and then increases. The corresponding ammonia yield is 5.5 μg mg_{cat}^{-1} h^{-1} with a Faradaic efficiency of 3.8%, as reported in Fig. 6c. After CA1, a new scan (labeled as CV2 in Fig. 6a) was performed adopting a wider range, from +0.07 vs RHE to −0.63 V vs RHE. The CA measurement performed after CV2 (CA2 in Fig. 6b) shows a more stable behavior and a net increase in the ammonia yield rate. Indeed, the measured ammonia rate after CA2 is 24.28 μg mg_{cat}^{-1} h^{-1}, with a Faradaic efficiency of 15.4% (see Fig. 6c), very large compared to the result obtained on the same electrode after CA1, i.e. after cycling in a narrower and less negative voltage range.

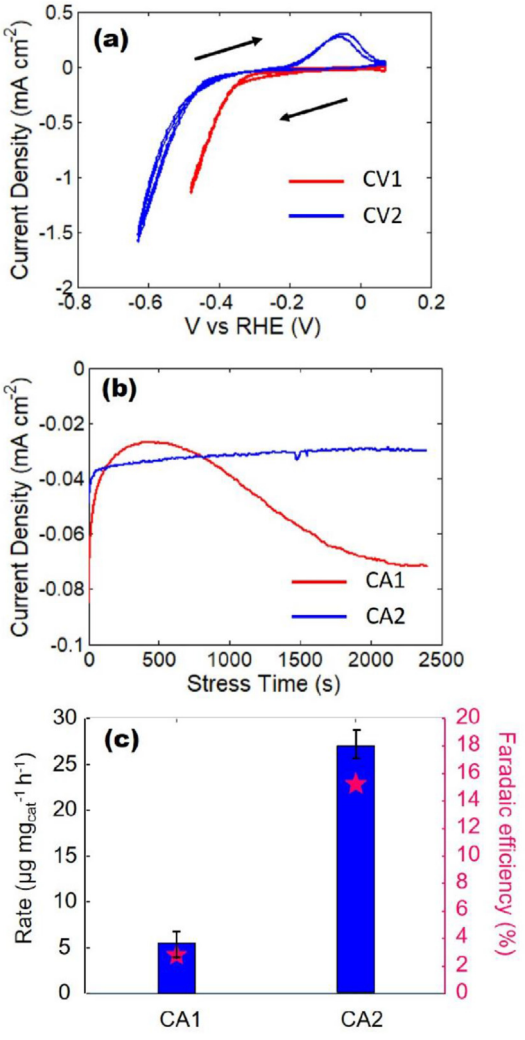

Fig. 6 − (a) Cyclic voltammetry obtained with 1 mM $FeCl_3$ scanning the potential from +0.07 to −0.45 V vs RHE (red) and from +0.07 to −0.63 V vs RHE (blue), (b) chronoamperometry at −0.33 V measured after CV1 (CA1 red curve) and CV2 (CA2 blue curve), and (c) NH_3 yield rate and Faradaic efficiencies obtained by performing CA1 or CA2. (For interpretation of the references to color in this figure legend, the reader is referred to the Web version of this article.)

Such an activation procedure has been also applied to the other samples produced with higher Fe concentration in the deposition solution, obtaining similar results, although with less improvement in the yield. As an example, for the sample treated with 2 mM $FeCl_3$ (see Fig. SI 7) after the activation procedure the rate increases from 3.3 to 6.6 μg mg_{cat}^{-1} h^{-1} and the Faradaic Efficiency is doubled, changing from 6% to 12%. In contrast, no relevant improvement in the yield upon activation has been obtained for 10 mM sample and for annealed 1 mM (Figs. SI 8 and SI 9). In both these two latter cases an almost uniform film was obtained at the carbon cloth surface, instead of nanoparticles.

In order to better investigate the activation mechanisms, and to understand if it takes place during the CV2 (with extended range) or the chronoamperometry, the catalyst activity has been measured by EASA in as deposited fresh catalyst (without performing any CV), after a chronoamperometry at −0.33 V vs RHE (CA0) performed without being preceded by any CV, and after CV2. The results are reported in Fig. 7. The double layer capacitance of the as deposited catalyst, equal to 7.6 mF cm^{-2}, increases up to 11.7 mF cm^{-2} after CV2. The CA0, instead, does not produce any significant change. The comparison between CA0, CA1 and CA2 is shown in Fig. SI 10. Indeed, CA of the fresh sample (without performing any CV) is very similar to that of the sample after CV1, therefore confirming that the activation only occurs after CA2. These results clearly indicate that an increased active area can be obtained by the extended cyclic voltammetry (CV2), which can then be considered as a suitable activation procedure.

According to the iron Pourbaix diagram [53] (see SI 11), in the negative voltage range, at the cathode side at pH of about 7, two reactions are expected to occur [54]. Indeed, at 0 V the most stable compound is Fe_2O_3 (Fe^{+3}) but it changes in Fe_3O_4 (with Fe^{+3} and Fe^{+2}) at about-0.15 V vs RHE and then in Fe at −0.5 vs RHE.

In order to obtain more insight on the structural changes induced by the activation process we acquired the XPS spectrum of the 1 mM sample after activation and drying.

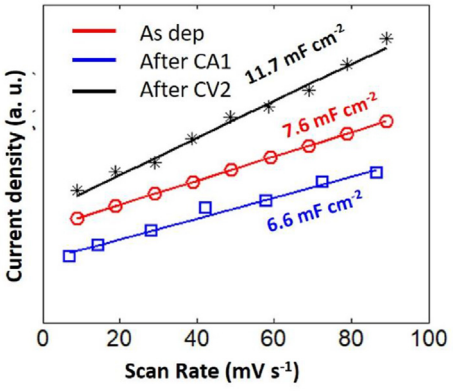

Fig. 7 − A comparison of electrical double layer capacitance before and after the CA1 and CV2.

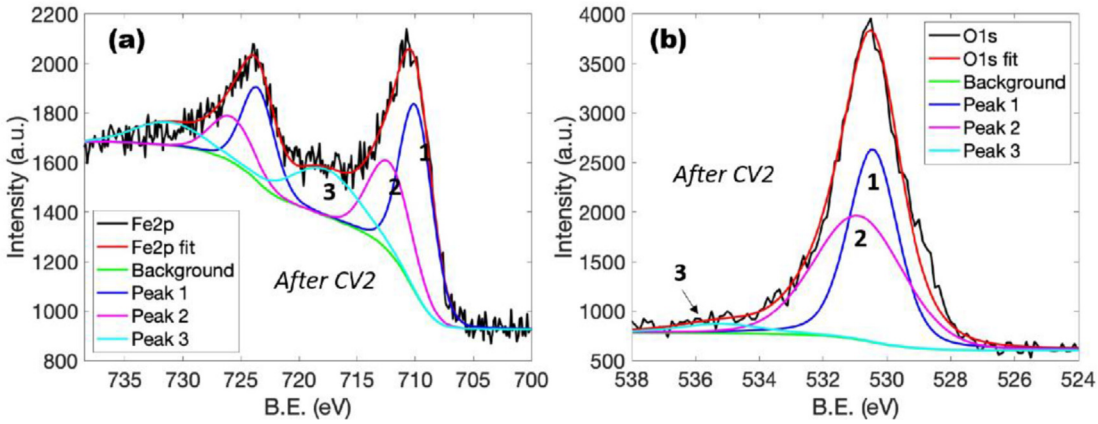

Fig. 8 – XPS spectra for Fe 2p in the 1 mM sample after cyclic voltammetry with data obtained by simulation.

Fig. 8a shows the Fe 2p spectra acquired after cyclic voltammetry in range 2 (CV2). As already seen for the as deposited sample (Fig. 5a) three peaks are obtained. The fitting data are reported in. After activation the contribution of peak 1 (Fe^{+2}) increases from 39% to 48%, that of peak 2 (Fe^{+3}) does not change and the satellite area decreases from 32% to 23%, suggesting an increase of the amount of reduced iron and a corresponding increase of the oxygen vacancies after cyclic voltammetry.

The O1s XPS peaks before and after (Fig. 8b) activation changed too. The small peak at 535.25eV binding energy (peak 3) is related to surface hydroxyl groups. We observed an increase in the oxygen vacancy peak (peak 1 at 531eV BE), the relative area increased from 41.5% to 49.7%, at the expense of that corresponding to the metal oxygen bond (peak 2 at 530eV BE), with a decrease in the relative area from 58.5% to 46.1%. Such a change improves the electrocatalytic activity of the layer thanks to a new asymmetric three dimensional electronic structure obtained after oxygen removal [52]. We therefore can conclude that (1) the activation process takes place by cyclic voltammetry in the extended range (+0.07 vs RHE to −0.63 V vs RHE) and (2) the activation produces an increase of the oxygen vacancies and Fe^{+2}/Fe^{+3}, with a corresponding increase of active sites available for the catalytic reaction. The effect of electrochemical activation is schematically summarized in Fig. 9.

The e-NRR mechanism is quite complex and still unclear, even if many efforts have been devoted to the elucidations of its highlights. Basically, it consists of three steps: i) N_2 adsorption at the active site; ii) hydrogenation and (iii) desorption of the NH_3 molecule. Once the N_2 approaches the surface, two paths are possible according to the predictions already present in the literature and based upon the breaking of the N≡N triple bond. In the dissociative mechanism the bond is broken during adsorption on the catalyst site, so, after hydrogenation, the surface is populated by NH_x species. In the associative pathway, instead, the N_2 molecule is broken after adsorption during the hydrogenation process and the catalyst sites are covered in principle with N_2H_x species [14]. The e-NRR mechanism associated to the TM materials is the associative Heyrovsky model, with catalytic sites populated by N_2H_x species [55]. The presence of oxygen vacancy, providing unsaturated sites for the N_2 adsorption and activation, may promote the hydrogenation process and the ammonia formation.

To evaluate the superior activity for e-NRR of the electrode loaded with 1 mM $FeCl_3$ we conducted chronoamperometry at different voltages in the range between −0.31 and −0.47 V vs RHE. Ar control experiments have been performed at each chronoamperometry. The amount of ammonia has been calculated as $(NH_3)_{produced} = NH_3(N_2) - NH_3(Ar)$. Data about experiments for all the prepared electrocatalysts are reported in Figs. SI 12-14 while the results for the best catalyst, activated Fe 1 mM are reported in Fig. 10a-b. The NH_3 yield rate is maximum at −0.35 V vs RHE with 26.44 $\mu g\, mg_{cat}^{-1}\, h^{-1}$ and a corresponding Faradaic Efficiency of 20.4%. The same catalyst has been employed to perform the NRR for several times at different voltages. Repetition at the same voltage clearly indicates that the ammonia yield does not change after seven consecutive electrolysis cycles (Fig. SI15), indicating that the catalytic performance is well-maintained, and the stability is good.

Thanks to the adopted strategy to optimize the morphology and improve the catalytic sites by an electrochemical activation process, we have been able to achieve good results compared to literature and to find a viable way to improve the electrocatalytic activity of iron-based catalysts

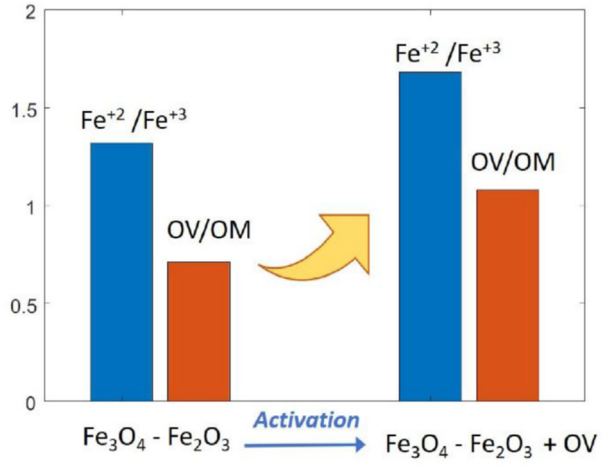

Fig. 9 – Schematic of the effect of activation process.

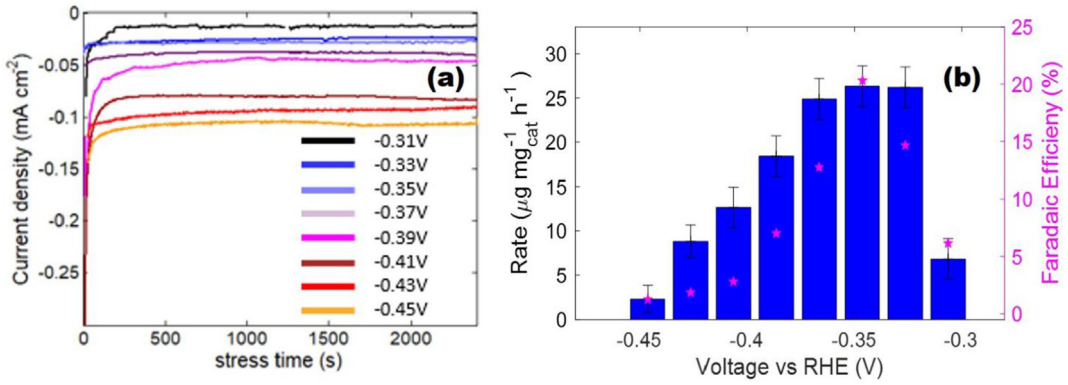

Fig. 10 – e-NRR measurements for electrode obtained with 1 mM $FeCl_3$ electrode: (a) chronoamperometry results and (b) average NH_3 yield rate and Faradaic efficiencies at a given potentials.

for ammonia electrosynthesis. A comparison is reported in Table 1.

Conclusions

The NRR catalytic properties of Fe-oxide based nanoparticles obtained by solution-based deposition on carbon cloth electrodes have been studied for different morphologies. The ammonia production yield and faradaic efficiency can be improved by adopting a strategy based on optimization of the morphology and electrochemical activity. By electrochemical and structural analyses, we have demonstrated that the nanoparticle size and the oxygen vacancy are crucial factors in determining the activity of iron oxide based catalysts for NRR, giving insight for designing more efficient materials.

Declaration of competing interest

The authors declare that they have no known competing financial interests or personal relationships that could have appeared to influence the work reported in this paper.

Acknowledgements

This research was funded by the European project TELEGRAM. The project has received funding from the European Union's Horizon 2020 Research and Innovation Programme under grant agreement No 101006941. The authors thank the Bionanotech Research and Innovation Tower (BRIT) laboratory and the project: "Piano della ricerca di Ateneo 2020-22 linea 2" of the University of Catania for the Smartlab diffractometer and financial support.

Appendix A. Supplementary data

Supplementary data to this article can be found online at https://doi.org/10.1016/j.ijhydene.2023.03.241.

REFERENCES

[1] Yu S, Wang Q, Wang J, Xiang Y, Niu X, Li T. Zinc doped Fe_2O_3 for boosting Electrocatalytic Nitrogen Fixation to ammonia under mild conditions. Int J Hydrogen Energy 2021;46:14331–7. https://doi.org/10.1016/J.IJHYDENE.2021.01.180.

[2] Klaas L, Guban D, Roeb M, Sattler C. Recent progress towards solar energy integration into low-pressure green ammonia production technologies. Int J Hydrogen Energy 2021;46:25121–36. https://doi.org/10.1016/J.IJHYDENE.2021.05.063.

[3] Makhloufi C, Kezibri N. Large-scale decomposition of green ammonia for pure hydrogen production. Int J Hydrogen Energy 2021;46:34777–87. https://doi.org/10.1016/J.IJHYDENE.2021.07.188.

[4] Smith C, Hill AK, Torrente-Murciano L. Current and future role of Haber–Bosch ammonia in a carbon-free energy landscape. Energy Environ Sci 2020;13:331–44. https://doi.org/10.1039/C9EE02873K.

[5] Fernandez CA, Hatzell MC. Editors' choice—economic considerations for low-temperature electrochemical ammonia production: achieving Haber-Bosch parity. J Electrochem Soc 2020;167:143504. https://doi.org/10.1149/1945-7111/ABC35B.

[6] Bicer Y, Dincer I, Zamfirescu C, Vezina G, Raso F. Comparative life cycle assessment of various ammonia production methods. J Clean Prod 2016;135:1379. https://doi.org/10.1016/j.jclepro.2016.07.023.

[7] Faria JA. Renaissance of ammonia synthesis for sustainable production of energy and fertilizers. Curr Opin Green Sustain Chem 2021;29:100466. https://doi.org/10.1016/J.COGSC.2021.100466.

[8] Liu A, Yang Y, Ren X, Zhao Q, Gao M, Guan W, et al. Current progress of electrocatalysts for ammonia synthesis through electrochemical nitrogen reduction under ambient conditions. Chem Sus Chem 2020;13:3766–88. https://doi.org/10.1002/CSSC.202000487.

[9] Tang C, Qiao SZ. How to explore ambient electrocatalytic nitrogen reduction reliably and insightfully. Chem Soc Rev 2019;48:3166–80. https://doi.org/10.1039/C9CS00280D.

[10] Yang X, Ma Y, Liu Y, Wang K, Wang Y, Liu M, et al. Defect-induced Ce-doped Bi_2WO_6 for efficient electrocatalytic N2 Reduction. ACS Appl Mater Interfaces 2021;13:19864–72. https://doi.org/10.1021/ACSAMI.0C22623.

[11] Majumder M, Saini H, Dědek I, Schneemann A, Chodankar NR, Ramarao V, et al. Rational design of graphene

derivatives for electrochemical reduction of nitrogen to ammonia. ACS Nano 2021;15:17275–98. https://doi.org/10.1021/ACSNANO.1C08455.
[12] Wang B, Huang S, Yang L, Fu Q, Bu Y. Regulating the catalytic performance of a dual-atom iron species deposited on graphitic carbon nitride for electrochemical nitrogen reduction. J Phys Chem C 2021;125:14253–62. https://doi.org/10.1021/ACS.JPCC.1C02397.
[13] Song P, Kang L, Wang H, Guo R, Wang R. Nitrogen (N), phosphorus (P)-Codoped porous carbon as a metal-free electrocatalyst for N_2 reduction under ambient conditions. ACS Appl Mater Interfaces 2019;11:12408–14. https://doi.org/10.1021/acsami.8b20472.
[14] Feng J, Pan H. Electronic state optimization for electrochemical N_2 reduction reaction in aqueous solution. J Mater Chem 2020;8:13896–915. https://doi.org/10.1039/D0TA04709K.
[15] Hui X, Wang L, Yao Z, Hao L, Sun Z. Recent progress of photocatalysts based on tungsten and related metals for nitrogen reduction to ammonia. Front Chem 2022;10:959. https://doi.org/10.3389/FCHEM.2022.978078.
[16] Wang H, Yang D, Liu S, Yin S, Yu H, Xu Y, et al. Amorphous sulfur decorated gold nanowires as efficient electrocatalysts toward ambient ammonia synthesis. ACS Sustainable Chem Eng 2019;7(24):19969–74.
[17] Shi MM, Bao D, Wulan BR, Li YH, Zhang YF, Yan JM, et al. Au sub-nanoclusters on TiO_2 toward highly efficient and selective electrocatalyst for N_2 conversion to NH_3 at ambient conditions. Adv Mater 2017;29:1606550. https://doi.org/10.1002/ADMA.201606550.
[18] Wang H, Yu H, Wang Z, Li Y, Xu Y, Li X, et al. Electrochemical fabrication of porous Au film on Ni foam for nitrogen reduction to ammonia. Small 2019;15:1804769. https://doi.org/10.1002/SMLL.201804769.
[19] Qin Q, Heil T, Antonietti M, Oschatz M. Single-site gold catalysts on hierarchical N-doped porous noble carbon for enhanced electrochemical reduction of nitrogen. Small Methods 2018;2:1800202. https://doi.org/10.1002/SMTD.201800202.
[20] Liu A, Yang Q, Ren X, Gao M, Yang Y, Gao L, et al. Two-dimensional CuAg/Ti_3C_2 catalyst for electrochemical synthesis of ammonia under ambient conditions: a combined experimental and theoretical study. Sustain Energy Fuels 2020;4:5061–71. https://doi.org/10.1039/D0SE00915F.
[21] Xu Y, Ren T, Yu S, Ren K, Wang M, Wang Z, et al. Anchoring Au nanoparticles on Bi ultrathin nanosheets for use as an efficient heterogeneous catalyst for ambient-condition electrochemical ammonia synthesis. Sustain Energy Fuels 2020;4:4516–21. https://doi.org/10.1039/D0SE00764A.
[22] Liu Chengchen, Li Shaoxiong, Li Zerong, Zhang Longcheng, Chen Haijun, Zhao Donglin, et al. Ambient N_2 to NH_3 fixation over a CeO_2 nanoparticle decorated three-dimensional carbon skeleton. Sustain. Energy Fuels 2022;6:3344–8. https://doi.org/10.1039/D2SE00557C.
[23] Ye K, He Z, Wu F, Wang Y, Wang L, Cheng Y, et al. Carbon nitride-supported $CuCeO_2$ composites derived from bimetal MOF for efficiently electrocatalytic nitrogen fixation. Int J Hydrogen Energy 2021;46:35319–29. https://doi.org/10.1016/J.IJHYDENE.2021.08.097.
[24] Wu L, Ji Y, Dai D, Chen T, Yang D, Liu Y, et al. Exceptional size-dependent activity enhancement in the catalytic electroreduction of N_2 over Mo nanoparticles. Int J Hydrogen Energy 2020;45:31841–8. https://doi.org/10.1016/J.IJHYDENE.2020.08.173.
[25] Hu L, Khaniya A, Wang J, Chen G, Kaden WE, Feng X. Ambient electrochemical ammonia synthesis with high selectivity on Fe/Fe oxide catalyst. ACS Catal 2018;8:9312–9. https://doi.org/10.1021/acscatal.8b02585.
[26] Cui B, Zhang J, Liu S, Liu X, Xiang W, Liu L, et al. Electrochemical synthesis of ammonia directly from N_2 and water over iron-based catalysts supported on activated carbon. Green Chem 2017;19:298–304. https://doi.org/10.1039/C6GC02386J.
[27] Liu Q, Zhang X, Zhang B, Luo Y, Cui G, Xie F, et al. Ambient N_2 fixation to NH_3 electrocatalyzed by a spinel Fe_3O_4 nanorod. Nanoscale 2018;10:14386–9. https://doi.org/10.1039/C8NR04524K.
[28] Li C, Fu Y, Wu Z, Xia J, Wang X. Sandwich-like reduced graphene oxide/yolk–shell-structured Fe@Fe_3O_4/carbonized paper as an efficient freestanding electrode for electrochemical synthesis of ammonia directly from H_2O and nitrogen. Nanoscale 2019;11:12997–3006. https://doi.org/10.1039/C9NR02782C.
[29] Lü F, Zhao S, Guo R, He J, Peng X, Bao H, et al. Nitrogen-coordinated single Fe sites for efficient electrocatalytic N_2 fixation in neutral media. Nano Energy 2019;61:420–7. https://doi.org/10.1016/J.NANOEN.2019.04.092.
[30] Cui X, Tang C, Liu XM, Wang C, Ma W, Zhang Q. Highly selective electrochemical reduction of dinitrogen to ammonia at ambient temperature and pressure over iron oxide catalysts. Chem Eur J 2018;24:18494–501. https://doi.org/10.1002/CHEM.201800535.
[31] Kim D, Surendran S, Lim Y, Choi H, Lim J, Kim JY, et al. Spinel-type Ni_2GeO_4 electrocatalyst for electrochemical ammonia synthesis via nitrogen reduction reaction under ambient conditions. Int J Energy Res 2022;46:4119–29. https://doi.org/10.1002/ER.7414.
[32] Kim D, Surendran S, Janani G, Lim Y, Choi H, Han MK, et al. Nitrogen-impregnated carbon-coated TiO_2 nanoparticles for N_2 reduction to ammonia under ambient conditions. Mater Lett 2022;314:131808. https://doi.org/10.1016/J.MATLET.2022.131808.
[33] Yu MS, Jesudass SC, Surendran S, Kim JY, Sim U, Han MK. Synergistic interaction of MoS2Nanoflakes on $La_2Zr_2O_7$Nanofibers for improving photoelectrochemical nitrogen reduction. ACS Appl Mater Interfaces 2022;14:31889–99. https://doi.org/10.1021/ACSAMI.2C05653.
[34] Kim D, Alam K, Han MK, Surendran S, Lim J, Young Kim J, et al. Manipulating wettability of catalytic surface for improving ammonia production from electrochemical nitrogen reduction. J Colloid Interface Sci 2023;633:53–9. https://doi.org/10.1016/J.JCIS.2022.11.052.
[35] Javaid R, Nanba T. Efficient Ru/MgO–CeO_2 catalyst for ammonia synthesis as a hydrogen and energy carrier. Int J Hydrogen Energy 2022. https://doi.org/10.1016/J.IJHYDENE.2022.05.280.
[36] El-Shafie M, Kambara S. Recent advances in ammonia synthesis technologies: toward future zero carbon emissions. Int J Hydrogen Energy 2022. https://doi.org/10.1016/J.IJHYDENE.2022.09.061.
[37] Wang B, Yin X, Wang P, Shen L. Chemical looping ammonia synthesis at atmospheric pressure benefiting from synergistic effect of Mn- and Fe-based nitrogen carriers. Int J Hydrogen Energy 2023;48:2705–17. https://doi.org/10.1016/J.IJHYDENE.2022.10.132.
[38] Huang YK, Jena A, Chen YT, Fang MH, Yang NH, Chang H, et al. Nanosized-Fe_3PtN supported on nitrogen-doped carbon as electro-catalyst for oxygen reduction reaction. Int J Hydrogen Energy 2017;42:15761–9. https://doi.org/10.1016/J.IJHYDENE.2017.03.175.
[39] Liu H, Guijarro N, Luo J. The pitfalls in electrocatalytic nitrogen reduction for ammonia synthesis. J Energy Chem 2021;61:149–54. https://doi.org/10.1016/J.JECHEM.2021.01.039.

[40] Li L, Tang C, Yao D, Zheng Y, Qiao SZ. Electrochemical nitrogen reduction: identification and elimination of contamination in electrolyte. ACS Energy Lett 2019;4:2111–6. https://doi.org/10.1021/ACSENERGYLETT.9B01573.
[41] Ren Y, Yu C, Tan X, Han X, Huang H, Huang H, et al. Is it appropriate to use the nafion membrane in electrocatalytic N_2 reduction? Small Methods 2019;3:1900474. https://doi.org/10.1002/SMTD.201900474.
[42] Leonardi M, Tranchida G, Corso R, Milazzo RG, Lombardo SA, Privitera SMS. Role of the membrane transport mechanism in electrochemical nitrogen reduction experiments. Membranes 2022;12:969. https://doi.org/10.3390/MEMBRANES12100969. 2022;12:969.
[43] Andersen SZ, Čolić V, Yang S, Schwalbe JA, Nielander AC, McEnaney JM, et al. A rigorous electrochemical ammonia synthesis protocol with quantitative isotope measurements. Nature 2019;570(7762):504–8. https://doi.org/10.1038/s41586-019-1260-x.
[44] Zhao Y, Shi R, Bian X, Zhou C, Zhao Y, Zhang S, et al. Ammonia detection methods in photocatalytic and electrocatalytic experiments: how to improve the reliability of NH_3 production rates? Adv Sci 2019;6:1802109. https://doi.org/10.1002/ADVS.201802109.
[45] Milazzo RG, Privitera SMS, Scalese S, Monforte F, Bongiorno C, Condorelli GG, et al. Ultralow loading electroless deposition of IrO_x on nickel foam for efficient and stable water oxidation catalysis. Int J Hydrogen Energy 2020;45:26583–94. https://doi.org/10.1016/j.ijhydene.2020.07.049.
[46] Almeida TP, Kasama T, Muxworthy AR, Williams W, Nagy L, Hansen TW, et al. Visualized effect of oxidation on magnetic recording fidelity in pseudo-single-domain magnetite particles. Nat Commun 2014;5:1–6. https://doi.org/10.1038/ncomms6154.
[47] Tzitzios VK, Bakandritsos A, Georgakilas V, Basina G, Boukos N, Bourlinos AB, et al. Large-scale synthesis, size control, and anisotropic growth of γ-Fe_2O_3 nanoparticles: organosols and hydrosols. J Nanosci Nanotechnol 2007;7:2753–7. https://doi.org/10.1166/JNN.2007.605.
[48] Iyengar SJ, Joy M, Maity T, Chakraborty J, Kotnala RK, Ghosh S. Colloidal properties of water dispersible magnetite nanoparticles by photon correlation spectroscopy. RSC Adv 2016;6:14393–402. https://doi.org/10.1039/C5RA26488J.
[49] Yamashita T, Hayes P. Analysis of XPS spectra of Fe^{2+} and Fe^{3+} ions in oxide materials. Appl Surf Sci 2008;254:2441–9. https://doi.org/10.1016/J.APSUSC.2007.09.063.
[50] Poulin S, França R, Moreau-Bélanger L, Sacher E. Confirmation of X-ray photoelectron spectroscopy peak attributions of nanoparticulate iron oxides, using symmetric peak component line shapes. J Phys Chem C 2010;114:10711–8. https://doi.org/10.1021/JP100964X.
[51] Ying H, Chen T, Zhang C, Bi J, Li Z, Hao J. Regeneration of porous Fe_3O_4 nanosheets from deep eutectic solvent for high-performance electrocatalytic nitrogen reduction. J Colloid Interface Sci 2021;602:64–72. https://doi.org/10.1016/J.JCIS.2021.05.185.
[52] Sang Y, Cao X, Ding G, Guo Z, Xue Y, Li G, et al. Constructing oxygen vacancy-enriched Fe_2O_3@NiO heterojunctions for highly efficient electrocatalytic alkaline water splitting. CrystEngComm 2021;24:199–207. https://doi.org/10.1039/D1CE01309B.
[53] Perry SC, Gateman SM, Stephens LI, Lacasse R, Schulz R, Mauzeroll J. Pourbaix diagrams as a simple route to first principles corrosion simulation. J Electrochem Soc 2019;166:C3186–92. https://doi.org/10.1149/2.0111911JES.
[54] Beverskog B, Puigdomenech I. Revised pourbaix diagrams for iron at 25–300 °C. Corrosion Sci 1996;38:2121–35. https://doi.org/10.1016/S0010–938X(96)00067-4.
[55] Skúlason E, Bligaard T, Gudmundsdóttir S, Studt F, Rossmeisl J, Abild-Pedersen F, et al. A theoretical evaluation of possible transition metal electro-catalysts for N_2 reduction. Phys Chem Chem Phys 2011;14:1235–45. https://doi.org/10.1039/C1CP22271F.
[56] Wang Z, Zheng K, Liu S, Dai Z, Xu Y, Li X, et al. Electrocatalytic nitrogen reduction to ammonia by Fe_2O_3 nanorod array on carbon cloth. ACS Sustainable Chem Eng 2019;7:11754–9. https://doi.org/10.1021/ACSSUSCHEMENG.9B01991.
[57] Xiang X, Wang Z, Shi X, Fan M, Sun X. Ammonia synthesis from electrocatalytic N_2 reduction under ambient conditions by Fe_2O_3 nanorods. ChemCatChem 2018;10:4530–5. https://doi.org/10.1002/CCTC.201801208.
[58] Song P, Wang H, Cao X, Liu N, Wang Q, Wang R. Ambient electrochemical N_2 reduction to NH_3 on nitrogen and phosphorus Co-doped porous carbon with trace iron in alkaline electrolytes. Chemelectrochem 2020;7:212–6. https://doi.org/10.1002/CELC.201901786.
[59] Cui X, Tang C, Liu XM, Wang C, Ma W, Zhang Q. Highly selective electrochemical reduction of dinitrogen to ammonia at ambient temperature and pressure over iron oxide catalysts. Chem Eur J 2018;24:18494–501. https://doi.org/10.1002/CHEM.201800535.
[60] Wang M, Li F, Liu J. Glycerine-based synthesis of a highly efficient Fe_2O_3 electrocatalyst for N_2 fixation. RSC Adv 2020;10:29575–9. https://doi.org/10.1039/D0RA05831A.
[61] Wang F, Xia L, Li X, Yang W, Zhao Y, Mao J. Nano-ferric oxide embedded in graphene oxide: high-performance electrocatalyst for nitrogen reduction at ambient condition. Energy & Environmental Materials 2021;4:88–94. https://doi.org/10.1002/EEM2.12100.
[62] He X, Guo H, Zhang X, Liao T, Zhu Y, Tang H, et al. Facile electrochemical fabrication of magnetic Fe_3O_4 for electrocatalytic synthesis of ammonia used for hydrogen storage application. Int J Hydrogen Energy 2021;46:24128–34. https://doi.org/10.1016/J.IJHYDENE.2021.04.203.
[63] Wang Y, Cui X, Zhao J, Jia G, Gu L, Zhang Q, et al. Rational design of Fe–N/C hybrid for enhanced nitrogen reduction electrocatalysis under ambient conditions in aqueous solution. 2018. https://doi.org/10.1021/acscatal.8b03802.